# MAPPING SURFACE HOAR FROM NEAR-INFRARED REFLECTANCE TEXTURE IN A COLD LABORATORY ENVIRONMENT

James W. Dillon[1]*, Evan N. Schehrer[1], Chris P. Donahue[2], Karl W. Birkeland[3], and Kevin D. Hammonds[1]

[1]*Department of Civil Engineering, Montana State University, Bozeman, MT, USA*
[2]*Department of Geography, Earth, and Environmental Sciences, University of Northern British Columbia, Prince George, British Columbia, Canada*
[3]*USDA Forest Service, National Avalanche Center, Bozeman, MT, USA*

ABSTRACT: Surface hoar crystals are snow grains that form when water vapor deposits on the snow surface. Once buried, surface hoar is a prominent concern in the avalanche forecasting community. The formation and persistence of surface hoar are highly variable in space and time. Therefore, surface hoar detection is an ideal candidate for remote sensing. Though the near-infrared (NIR) reflectance of snow is sensitive to microstructure, previous studies have fallen short in their efforts to utilize NIR reflectance for delineation of surface hoar. We hypothesize that NIR texture, as opposed to reflected magnitude, may produce an optical signature unique to surface hoar. We tested this by performing a reflectance experiment in a controlled cold laboratory environment to evaluate the accuracy of surface hoar mapping from NIR texture using a near-infrared hyperspectral imager (NIR-HSI). We analyzed thirty snow samples with widely varying microstructure and found that surface hoar exhibited greater median values of a texture metric than other samples. Leveraging this finding, we created a simple binary classification algorithm to map the extent of surface hoar on a pixelwise basis. The algorithm proved sufficient, particularly at the central spatial resolution of 5 mm, with a median accuracy of 96.5%. Last, we underwent a repeatability test with resulting accuracy upwards of 99%. As NIR-HSI detectors become increasingly available, our findings may play a key role in remotely assessing the spatiotemporal variability of surface hoar, which could provide a critically important tool for avalanche forecasters.

KEYWORDS: Surface hoar, hyperspectral imagery, near-infrared, mapping, texture, remote sensing.

## 1. INTRODUCTION AND BACKGROUND

Mountainous and polar snowpacks are commonly blanketed by surface hoar, unique ice crystals that grow when water vapor deposits on the snow surface (Horton and Jamieson, 2017). Essentially the winter equivalent of dew, surface hoar crystals can grow to several centimeters in length and stand vertically atop the snow surface. Since snow albedo is largely controlled by surface microstructure, the formation, distribution, and disappearance of surface hoar affects the reflective properties of the ice-air interface and thus has a key influence on Earth's radiative energy budget (Champollion et al., 2013). Furthermore, surface hoar is a prominent concern for avalanche forecasters. Avalanches release on weak failure layers, typically when an interface with minimal cohesion or a layer with weak shear strength is loaded. The latter case describes surface hoar. Once buried, surface hoar layers are prone to fracture propagation and avalanche release (Horton and Jamieson, 2017; Jamieson and Schweizer, 2000). For instance, Birkeland (1998) found that nearly one-third of large natural avalanches in southwestern Montana failed on a layer of buried surface hoar. The formation and disappearance of surface hoar are highly variable in space and time, and difficult to predict due to complex distributions of precipitation, wind, radiation and vegetation encountered in polar and mountainous environments. The spatial distribution of surface hoar formation can vary on a subslope scale; temporally it can be promptly destroyed by environmental influences, or it can persist for weeks (Champollion et al., 2013; Lutz and Birkeland, 2011). Therefore, the detection of surface hoar is an ideal phenomenon to monitor with remote sensing.

Despite advances in snow optics, Horton and Jamieson (2017) note the fundamental disconnect between snow surface characterizations conducted by the remote sensing community (i.e., mapping of SSA, or similarly effective snow grain size, $r_e$, using near-infrared (NIR) reflectance), and the physical properties relevant to avalanche release. For avalanche forecasters, characterizing snow surface microstructure with the morphological grain shapes defined in the International Classification for Seasonal Snow on the Ground (ICSSG, Fierz et al., 2009) and their associated mechanical properties is critically important. Hence, a forecaster would much prefer a map of the presence of weak layers like surface hoar than a map of $r_e$. Relating morphological grain shape to $r_e$ is difficult because effective grain size is a complex function of grain shape, traditional grain size, bulk density, and other

physical characteristics. Therefore, $r_e$ is not particularly useful for avalanche forecasting operations. While certain magnitudes of $r_e$ are generally related to grain shape (Domine et al., 2007; Matzl and Schneebeli, 2010), few studies have formally attempted to use NIR reflectance for mapping morphological grain shape instead of $r_e$. Further, the studies that have attempted this (e.g., Bühler et al., 2014; Horton and Jamieson, 2017) have unfortunately found that surface hoar crystals produce very moderate reflectance signatures relative to other grain shapes, making them difficult to delineate from less-concerning snow structures based on NIR reflectance magnitude.

To the best of our knowledge, the only study to date that successfully identified surface hoar formation from NIR remote sensing was conducted by Champollion et al. (2013) in Antarctica. As opposed to evaluating magnitudes of NIR reflectance, the researchers leveraged a NIR texture signature, hence localized spatial variability in reflectance, to classify the presence of surface hoar using an infrared camera. Simply put, the researchers found that a large, localized variance in NIR reflectance, as quantified by a contrast index, was strongly correlated with surface hoar crystals. Here we postulate that the physical phenomenon for this finding is variable ice absorption and path length (Fig. 1). Depending on how an incoming photon interacts with the relatively large, often vertically oriented surface hoar crystals, the photon could experience a wide range of ice path lengths and thus absorption. All of this is before even considering the scattering and absorption properties of the underlying snow layer itself. As a result, *we hypothesize that the presence of surface hoar will coincide with a quantifiable increase in localized reflectance variance, a texture signature which could be used to map its distribution*. If this is the case, it would enable high spatial and temporal resolution mapping of surface hoar extent (prior to burial) in challenging environments, particularly as NIR remote sensors and unmanned aerial vehicles become more cost-effective. However, such a texture analysis has never been fully evaluated, rigorously quantified for accuracy, or compared to a wide variety of well-defined microstructures to ensure that the NIR texture is indeed a unique defining feature of surface hoar.

* *Corresponding author address:*
James W. Dillon, Montana State University, Bozeman, MT 59717; tel: +1 484-883-8933
email: james.dillon013@gmail.com

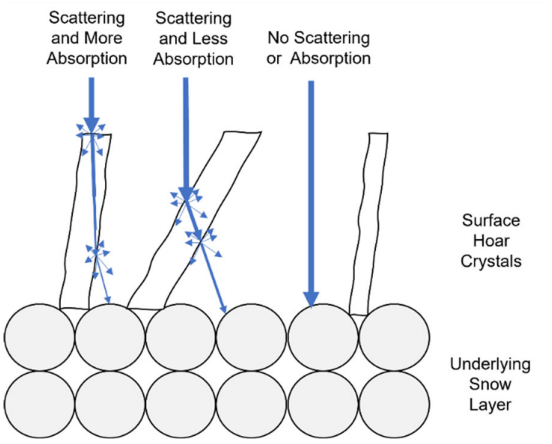


Figure 1: Idealized schematic of light scattering when encountering a surface hoar layer. Because surface hoar crystals are typically large and vertically oriented, incoming photons may experience a very long path length and thus substantial absorption before reaching the underlying snow layer (leftmost case). Depending on the angle of interaction, that path may be considerably shortened (middle case), or, as these crystals tend to be modestly spaced, photons may evade the surface hoar crystals entirely and pass straight into the underlying snow layer (rightmost case).

To address this knowledge gap, we performed an experiment in a controlled laboratory environment to determine if NIR texture can be used to delineate the extent of surface hoar. We first created snow samples with varying grain shapes and physical properties, and quantified their microstructures using X-ray computed microtomography (micro-CT). We then scanned each sample with a compact hyperspectral imager. We subsequently analyzed the resulting maps of reflectance to produce measurements of NIR texture. Finally, we used our results to inform optimal thresholds for the classification of surface hoar on a per-pixel basis, before analyzing the accuracy of our resulting classified data products.

## 2. METHODOLOGY

We aimed to create snow samples with a wide variety of well-defined grain shapes and microstructures, acquire optical data, and perform a texture analysis towards delineation of surface hoar from other snow surface structures. Section 2.1 describes sample preparation and physical characterization, Section 2.2 discusses acquisition of NIR-HSI data, Section 2.3 covers image texture analysis, and Section 2.4 describes classification.

### 2.1 Sample preparation and physical characterization

We underwent all sample preparation and assessment within Montana State University's Subzero Research Laboratory (SRL). Snow used in testing was a combination of laboratory-made grains produced in the SRL's snowmaking apparatus (much like the systems presented in Schleef et al. (2014) and Abe and Kosugi (2019)), as well as natural snow that we collected from the surrounding area. To ensure it was completely dry, we kept all snow in a cold room at -30° C and allowed it to equilibrate for at least 24 hours prior to evaluation. From twelve initial batches of varying snow grains (Fig. 2), we generated thirty snow samples by sieving snow through differing mesh sizes to further promote disparate microstructures. Sample grain habits included precipitation particles (PP), decomposing and fragmented precipitation particles (DF), rounded grains (RG), melt forms (MF), faceted crystals (FC), depth hoar (DH), and surface hoar (SH) (Fierz et al., 2009). We thoroughly characterized the properties of each sample using microscopy, a crystal card and hand lens, and micro-CT.

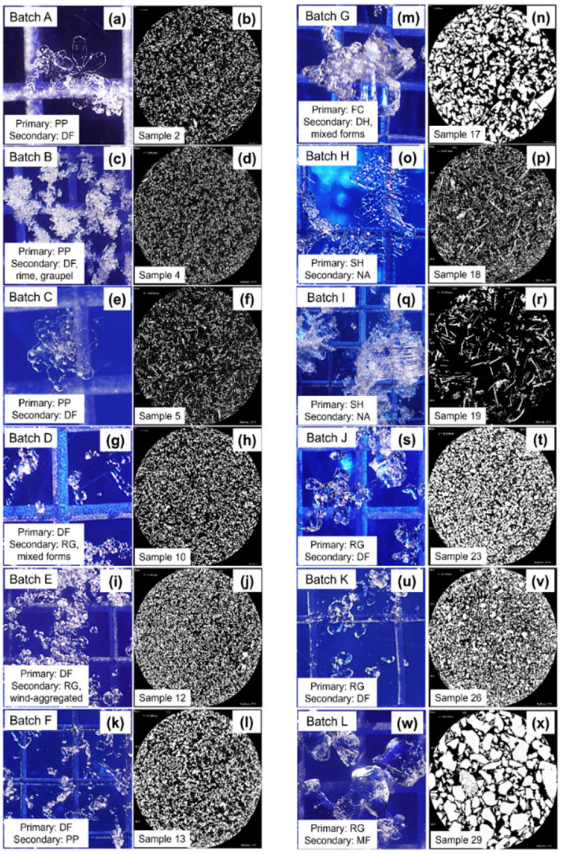


Figure 2: Microscopy images of grains from each initial batch (left columns) and binary micro-CT cross-sections from representative samples (right columns). In the microscopy images, the grid size on the underlying blue grain card is 2 mm.

### 2.2 Optical data acquisition

We used a Resonon Inc. Pika NIR-640 near-infrared hyperspectral imager to map snow reflectance in the NIR. Donahue et al. (2021) provide a detailed description of the instrument. Briefly, the imager's spectral resolution ranges from 2.39 to 2.50 nm, and measures 336 bands across the NIR region from 891–1711 nm. It constructs a 2D image containing the full spectrum in each pixel by collecting the image line by line, known commonly as a "push broom" or "line" scanner. Thus, to collect an image, the camera must move (translating or rotating) relative to the scene, or the scene must move relative to the imager. We used a Resonon benchtop linear scanning stage to move the sample beneath the sensor.

We positioned the hyperspectral imager above the linear translating stage that held the samples. For more details on the benchtop apparatus, see Donahue et al. (2022). The lens of the imager is surrounded by a set of four halogen lamps that produce direct illumination (Fig. 3a). The halogen lamps and lens of the imager are at a height of 38 and 47 cm above the snow surface, respectively. We used a Spectralon white diffuse reflectance panel for calibration, resulting in a bidirectional reflectance measurement (bidirectional reflectance factor, *R*) for each band in every individual pixel of the image.

Initial processing took place in Resonon's proprietary Spectronon software. We underwent analyses thereafter in R. We began by truncating the reflectance data to a central region-of-interest (ROI) encapsulating the micro-CT ROI (Fig. 3b). Resulting NIR-HSI ROIs contained 224,000 pix-

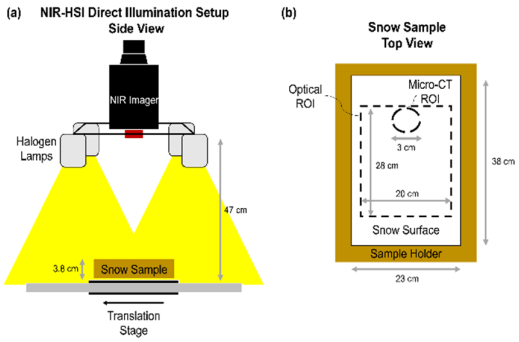


Figure 3: Laboratory data collection schematic for hyperspectral imaging (a). Data regions-of-interest within the snow sample are illustrated in (b).

els with a spatial resolution of 0.5 mm. To simplify processing, we elected to evaluate bidirectional reflectance from NIR-HSI at a single wavelength. Because this wavelength was selectable, we chose 1030 nm (hereafter $R_{1030}$), the center of the absorption feature. The last factor we sought to examine was spatial resolution, considering that if a NIR texture signature specific to surface hoar does exist, then it is likely resolution-dependent. Thus, we coarsened all NIR-HSI $R_{1030}$ datasets by two orders of magnitude (Fig. 4a – 4c), from 0.5 mm to resolutions of 5 mm and 5 cm, with an eye for mimicking the finer spatial resolutions achievable by UAV-mounted systems.

### 2.3 *Texture analysis*

To restate our hypothesis, we anticipated that surface hoar would display heightened NIR variability, or texture, relative to other snow surface types due to the physical phenomenon illustrated in Fig. 1. Therefore, we sought to evaluate localized variability of bidirectional reflectance. To achieve this, we performed a moving window focal analysis to create maps of local standard deviation. A demonstration of both coarsening and subsequent moving window analysis is presented in Fig. 4 for Sample 20. Beginning with a map of $R_{1030}$ at either the raw, 0.5 mm resolution (Fig. 4a), or a coarsened resolution (Fig. 4b – 4c), a square window with a length of three pixels is placed around a central pixel. The standard deviation of $R_{1030}$ (hereafter $\sigma_{1030}$) is calculated within the window, and the resulting value is assigned to the central pixel. Moving the window across each

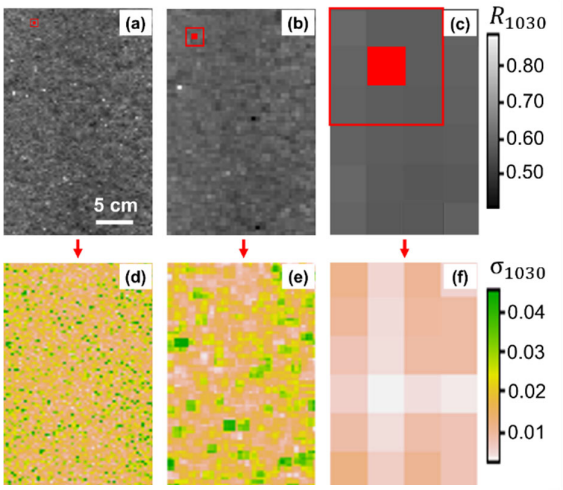


Figure 4: A map of $R_{1030}$ from NIR-HSI at its raw resolution of 0.5 mm (a) is coarsened by two orders of magnitude to 5 mm (b) and 5 cm (c). For each resolution, the localized standard deviation, $\sigma_{1030}$, is calculated using a three-pixel moving window analysis (d – f). The data shown is from Sample 20.

$R_{1030}$ map and evaluating every pixel independently yields a map of $\sigma_{1030}$ (Fig. 4d – 4f). Thus, these maps depict NIR reflectance texture, rather than magnitude. We compared distributions of σ and measures of central tendency across samples. We leveraged boxplots and line graphs for data visualization.

### 2.4 *Classification algorithm*

To produce classified maps of surface hoar, we investigated optimal threshold values of σ to delineate surface hoar from other snow surface types on a per-pixel basis. In addition to visualizing distributions (across all pixels) of σ with boxplots for each sample, we also constructed probability density functions (PDFs). For each spatial resolution, we grouped the distributions of surface hoar samples (Samples 18 – 20) and compared them to the grouped distributions of all other samples. We selected values of σ corresponding to the intersection of the grouped PDFs as the optimal thresholds of delineation for each resolution, termed $\sigma_{crit}$. We used these threshold values to perform a binary pixelwise classification; pixels with σ values above $\sigma_{crit}$ were classified as surface hoar, while values beneath were designated as "other" microstructures. We ran the classification algorithm on all samples using the appropriate $\sigma_{crit}$ value for each resolution. To evaluate the success of the classification algorithm, we calculated the true positive rate (TPR), true negative rate (TNR), and overall accuracy (A) for each sample using the following equations:

$$TPR = \frac{TP}{TP + FN} \quad (1)$$

$$TNR = \frac{TN}{TN + FP} \quad (2)$$

$$A = \frac{TN + TP}{TN + TP + FN + FP} \quad (3)$$

where TP is a true positive, TN is a true negative, etc. In this case, a TP refers to the correct identification of surface hoar when it is present, a TN corresponds to the correct identification of an "other" microstructure, a FP is when the algorithm makes an incorrect surface hoar classification, and a FN is when surface hoar is misclassified as "other".

Our final investigation was to test the spatial mapping capacity and repeatability of our texture-based classification on a new snow sample, one that was not involved in the initial analysis. Using the techniques outlined in Section 2.1, we grew surface hoar atop roughly *half* of the surface of a

rounded grain sample, while the other half remained covered. Thus, the resulting snow surface grain habit was a 1:1 ratio of SH:RG. We proceeded to run the classification algorithm on the mixed sample to produce a map of surface hoar extent.

## 3. RESULTS

### *3.1 Statistical analysis*

We found that surface hoar often exhibited larger values of $\sigma_{1030}$ relative to other sample microstructures, particularly at the two finer spatial resolutions (0.5 mm and 5 mm). This is illustrated by the line graph in Fig. 5, while also outlining the problem with using NIR reflectance magnitude to delineate surface hoar. At all three spatial resolutions, the median reflectance magnitude ($R_{1030}$) gradually increases proceeding from higher to lower sample numbers; this is sensible, as higher sample numbers tended to have lower SSA, and vice versa. This leaves the reflectance of surface hoar "hidden" in the middle. This lack of distinction is further outlined by the negligible difference between the median values of $R_{1030}$ for surface hoar (dotted black reference lines) and the median of all samples (solid black reference lines). When examining values of $\sigma_{1030}$ (red lines), very different patterns are evident. In Fig. 5a, median values of $\sigma_{1030}$ are fairly constant across all samples with the exception of surface hoar (Samples 18 – 20, highlighted in yellow), where a spike is present. The separation between the median value of $\sigma_{1030}$ for surface hoar samples (dotted red reference line) compared to all samples (solid red reference line) further illustrates this, and may allow for delineation of surface hoar based on this texture parameter. The distinction is even more pronounced at the coarser resolution of 5 mm (Fig. 5b), where the median $\sigma_{1030}$ value of all samples has declined while surface hoar values remain elevated. While this phenomenon is still observable at the spatial resolution of 5 cm (Fig. 5c), the effect is less pronounced and varies more between individual surface hoar samples. The performance of the 5 mm spatial resolution is further underscored by the boxplot in Fig. 6.

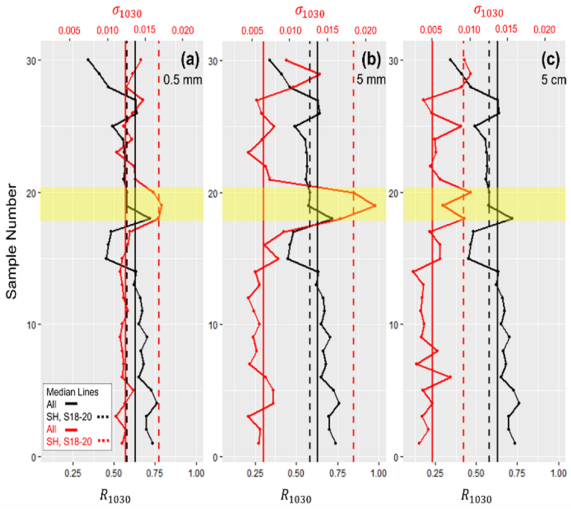


Figure 5: Sample median values of reflectance magnitude, $R_{1030}$ (lower x-axis), compared to reflectance texture, $\sigma_{1030}$ (upper x-axis), across all samples (y-axis). Panels a, b, and c correspond to spatial resolutions of 0.5 mm, 5 mm, and 5 cm, respectively. Solid vertical reference lines depict the median values of $R_{1030}$ or $\sigma_{1030}$ for all samples, while dotted reference lines are median values of only surface hoar samples (S18 – S20).

### *3.2 Classified data products*

We used PDFs to compare the density distributions of surface hoar samples (Samples 18 – 20) against all other samples, which allowed us to determine critical thresholds of $\sigma$ ($\sigma_{crit}$) for surface hoar delineation under each NIR-HSI spatial resolution. This process is illustrated in Fig. 7. Selecting the intersection point of the two distributions, following Champollion et al. (2013), allows for optimal binary classification of a given pixel. The resulting critical values for each condition are listed on the PDF plots. Using these $\sigma_{crit}$ values,

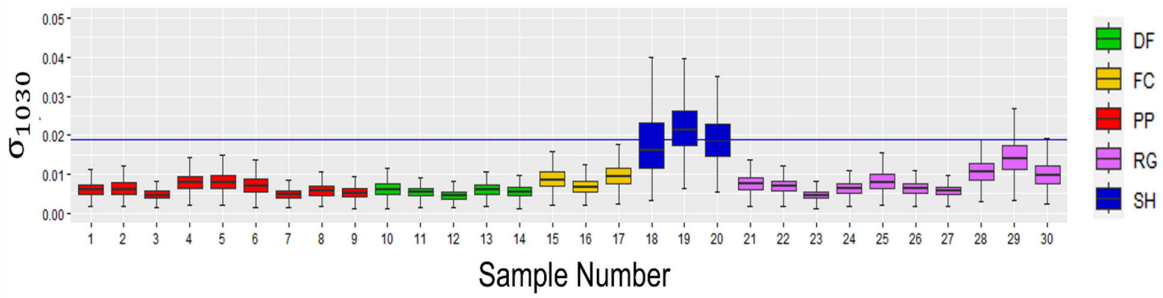


Figure 6: Samplewise boxplot analysis for the middle resolution of 5 mm, which performed the best. Boxes are colored by primary grain habit. Blue horizontal reference line depicts the median value of $\sigma$ for surface hoar Samples 18 – 20.

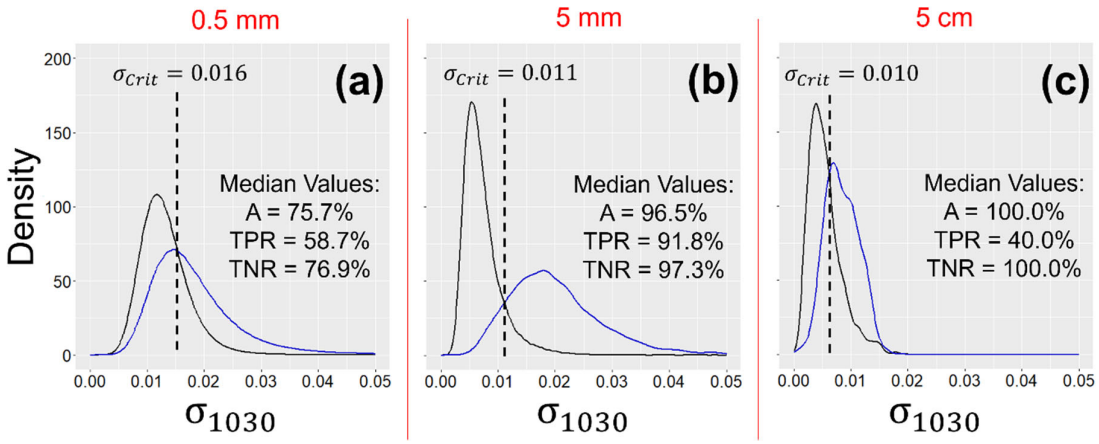


Figure 7: Probability density functions juxtaposing the $\sigma_{1030}$ distributions of surface hoar, Samples 18 – 20 (blue curves), with those of all other samples (black curves) for each spatial resolution. Dotted vertical reference lines represent he distribution intersection, where the critical threshold values ($\sigma_{crit}$) were extracted. Median accuracy metrics from the resulting samplewise binary classifications are also listed for each scenario.

we conducted pixelwise classification of all samples for each resolution. All sample-wise accuracy values (A) are listed in Table 1, while median values of A, TPR, and TNR for each scenario are included on the Fig. 7 PDF plots. Classification results generally mirrored those of the statistical analysis. That is, results were excellent at the finer spatial resolutions of 0.5 mm and especially 5 mm, but dwindled substantially (particularly in terms of TPR) at the coarser resolution of 5 cm. The classification algorithm struggled most with samples of a FC primary grain habit (Samples 15 – 17), as well as the largest RGs (Samples 28 – 30), but was proficient elsewhere.

Classification accuracy assessed on a new sample, comprised of a 1:1 ratio of RG and SH surface grain shapes, proved consistent, demonstrating repeatability of the texture phenomenon (Fig. 8). Further, we observe the capacity to map surface hoar extent amid mixed surface conditions. We selected the central NIR-HSI spatial resolution of 5 mm for evaluation, as this resolution performed best in the statistical and classification analyses. Correct rejection of the RG surface (hence TNR) was nearly perfect. Accurate identification of SH (i.e., TPR) was also excellent, but with notably more areas of discontinuous misclassification. This can likely be attributed to the relatively broad $\sigma_{1030}$ distribution of SH Samples 18 – 20 (Fig. 6).

| | $\sigma_{crit}$ | | |
|---|---|---|---|
| | 0.5 mm | 5 mm | 5 cm |
| | 0.016 | 0.011 | 0.010 |
| Sample | A (%) | | |
| # | 0.5 mm | 5 mm | 5 cm |
| 1 | 82.5 | 97.6 | 100.0 |
| 2 | 76.9 | 94.5 | 91.4 |
| 3 | 89.1 | 99.8 | 100.0 |
| 4 | 79.4 | 88.5 | 100.0 |
| 5 | 68.9 | 87.3 | 100.0 |
| 6 | 82.0 | 90.5 | 85.7 |
| 7 | 81.5 | 99.3 | 100.0 |
| 8 | 82.9 | 98.3 | 90.6 |
| 9 | 84.0 | 99.4 | 100.0 |
| 10 | 80.5 | 95.0 | 100.0 |
| 11 | 75.3 | 99.7 | 100.0 |
| 12 | 79.7 | 99.7 | 100.0 |
| 13 | 70.3 | 97.6 | 100.0 |
| 14 | 65.6 | 99.3 | 100.0 |
| 15 | 84.6 | 81.3 | 100.0 |
| 16 | 87.6 | 96.0 | 97.1 |
| 17 | 69.8 | 70.6 | 100.0 |
| 18 | 58.7 | 78.3 | 40.0 |
| 19 | 61.4 | 97.1 | 5.7 |
| 20 | 54.4 | 91.8 | 48.6 |
| 21 | 65.5 | 92.0 | 100.0 |
| 22 | 66.7 | 97.3 | 100.0 |
| 23 | 88.6 | 99.7 | 100.0 |
| 24 | 69.9 | 98.4 | 100.0 |
| 25 | 81.7 | 86.3 | 74.3 |
| 26 | 69.0 | 98.5 | 100.0 |
| 27 | 56.3 | 99.6 | 100.0 |
| 28 | 76.1 | 59.7 | 65.7 |
| 29 | 68.0 | 25.5 | 47.5 |
| 30 | 58.6 | 66.6 | 54.3 |
| **Median** | **75.7** | **96.5** | **100.0** |

Table 1: Sample-wise and median accuracy (A) values for each sample resolution. Results for surface hoar, Samples 18 – 20, are shaded in blue.

## 4. DISCUSSION AND CONCLUSIONS

We found that surface hoar exhibited higher values of $\sigma_{1030}$, a NIR texture metric, than other snow surface structures (PP, DF, FC, RG, and MF) when measured with NIR-HSI. Our findings are consistent with Champollion et al. (2013),

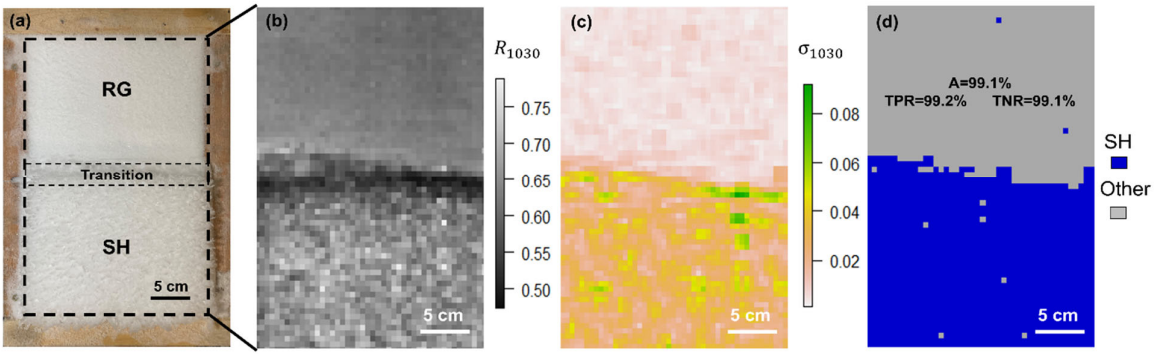


Figure 8: A sample with a 50:50 ratio of RG:SH surface grain habits is displayed in the visible (a). The bidirectional reflectance factor at 1030 nm is extracted (b) from NIR-HSI. Via a moving window analysis, localized standard deviation ($\sigma_{1030}$), or NIR texture, is quantified (c), and then binarized using critical thresholds to produce classified maps (d). Overall accuracy, true positive rates, and true negative rates are listed on the classified maps. The transitional zone was excluded in accuracy analyses.

who found that, under artificial lighting conditions, the NIR texture (in this case a contrast index) of the Antarctic snow surface was higher when surface hoar was present as compared to when it was absent. Our work builds on these foundational findings by quantifying the texture phenomenon against a variety of differing snow microstructures in a controlled laboratory environment and features the explicit inclusion of varied spatial resolutions. Further, whereas Champollion et al. (2013) used texture metrics across an entire image to confirm the presence of hoar crystals on a given day (with accuracy of 94%), we extend this classification by demonstrating a per-pixel mapping methodology, allowing us to map the spatial extent of surface hoar within an image (Fig. 8). As discussed in Section 3.1 and illustrated in Fig. 5, surface hoar exhibits middling NIR reflectance when compared to other grain habits, and thus leveraging reflectance magnitude alone is insufficient for surface hoar delineation. These results highlight the importance of our texture-based approach.

Although scaling to field applications presents considerable challenges and uncertainty, it is likely that our findings can be extended to operational avalanche forecasting in the near future. A simple setup like that of Champollion et al. (2013), where a downward-looking NIR camera acquired daily and nightly images, is not difficult to imagine, and could be constructed at a field site representative of an avalanche area. Such remote measurements would inform practitioners when surface hoar forms, whether or not it persists on the surface, and when it gets buried. This information would be critically important for avalanche forecasters. Further, texture analyses via UAV, and thus slope-scale mapping, are likely feasible in the not-too-distant future. Although differing illumination conditions and incidence angles would need to be accounted for, current UAV-mounted imaging systems can achieve the coarser spatial resolutions examined here. Maps of surface hoar extent over avalanche terrain prior to burial would be vital in making slope-specific avalanche forecasts, as well as informing the most likely trigger points on a slope, where practitioners may choose to place an explosive, for example.

Our research demonstrates the novel capacity of NIR-HSI for mapping the spatial extent of surface hoar from NIR texture in a cold laboratory. In essence, we found that:

i. Hyperspectral imaging can robustly measure the texture of snow and ice by computing pixelwise variability in reflectance at any NIR wavelength, such as the center of the 1030 nm ice absorption feature.

ii. When evaluated with NIR-HSI, surface hoar has heightened NIR texture relative to other snow microstructures, likely as a result of variable ice absorption.

iii. Near-infrared texture thresholds can be used to binarize NIR-HSI texture measurements, resulting in accurate maps of surface hoar spatial extent on a per-pixel basis.

As NIR-HSI becomes more economical, these may provide capable methods for measuring NIR texture and subsequently mapping surface hoar. Extending the work presented here to field

operations will have immediate implications for broad-scale snow surface mapping and avalanche forecasting.

## ACKNOWLEDGEMENTS

Funding for this project was provided in part by the Transportation Avalanche Research Pool. We would like to thank Resonon, Inc. for providing us with a hyperspectral imager and technical assistance. We acknowledge the use of the Subzero Research Laboratory at Montana State University, and especially thank Ladean McKittrick for laboratory assistance. The presented data are available upon request from the lead author.

## REFERENCES

Abe, O., & Kosugi, K.: Twenty-year operation of the Cryospheric Environment Simulator. *Bulletin of Glaciological Research*, *37*, 53-65, doi: 10.5331/bgr.16SR01, 2019.

Birkeland, K. W.: Terminology and predominant processes associated with the formation of weak layers of near-surface faceted crystals in the mountain snowpack. *Arctic and Alpine Research*, *30*(2), 193-199, DOI: 10.1080/00040851.1998.12002891, 1998.

Bühler, Y., Meier, L., & Ginzler, C.: Potential of operational high spatial resolution near-infrared remote sensing instruments for snow surface type mapping. *IEEE Geoscience and Remote Sensing Letters*, *12*(4), 821-825, DOI: 10.1109/LGRS.2014.2363237, 2014.

Champollion, N., Picard, G., Arnaud, L., Lefebvre, E., & Fily, M.: Hoar crystal development and disappearance at Dome C, Antarctica: observation by near-infrared photography and passive microwave satellite. *The Cryosphere*, *7*(4), 1247-1262, doi:10.5194/tc-7-1247-2013, 2013.

Domine, F., Taillandier, A. S., & Simpson, W. R.: A parameterization of the specific surface area of seasonal snow for field use and for models of snowpack evolution. *Journal of Geophysical Research: Earth Surface*, *112*(F2), doi:10.1029/2006JF000512, 2007.

Donahue, C., Skiles, S. M., & Hammonds, K.: In situ effective snow grain size mapping using a compact hyperspectral imager. *Journal of Glaciology*, *67*(261), 49-57, doi: 10.1017/jog.2020.68, 2021.

Donahue, C., Skiles, S. M., & Hammonds, K.: Mapping liquid water content in snow at the millimeter scale: an intercomparison of mixed-phase optical property models using hyperspectral imaging and in situ measurements. *The Cryosphere*, *16*(1), 43-59, doi: 10.5194/tc-16-43-2022, 2022.

Fierz, C. R. L. A., Armstrong, R. L., Durand, Y., Etchevers, P., Greene, E., McClung, D. M., ... & Sokratov, S. A. (2009). The international classification for seasonal snow on the ground.

Horton, S., & Jamieson, B.: Spectral measurements of surface hoar crystals. *Journal of Glaciology*, *63*(239), 477-486, doi: 10.1017/jog.2017.6, 2017.

Jamieson, J. B., & Schweizer, J.: Texture and strength changes of buried surface-hoar layers with implications for dry snow-slab avalanche release. *Journal of Glaciology*, *46*(152), 151-160, doi:10.3189/172756500781833278, 2000.

Lutz, E. R., & Birkeland, K. W.: Spatial patterns of surface hoar properties and incoming radiation on an inclined forest opening. *Journal of Glaciology*, *57*(202), 355-366, doi:10.3189/002214311796405843, 2011.

Matzl, M., & Schneebeli, M.: Stereological measurement of the specific surface area of seasonal snow types: Comparison to other methods, and implications for mm-scale vertical profiling. *Cold Regions Science and Technology*, *64*(1), 1-8, doi: 10.1016/j.coldregions.2010.06.006, 2010.

Schleef, S., Jaggi, M., Löwe, H., & Schneebeli, M.: An improved machine to produce nature-identical snow in the laboratory. *Journal of Glaciology*, *60*(219), 94-102, doi: 10.3189/2014JoG13J118, 2014.